An accelerated version of alternating direction method of multipliers for TV minimization in EIT

Ashkan Javaherian[a], Manuchehr Soleimani[b], Knut Moeller[a], Amir Movafeghi[c] , Reza Faghihi[d]

[a] Institute of Technical Medicine, Faculty of Medical and Life Sciences, Furtwangen University of Applied Sciences, Villingen‑Schwenningen, Germany
[b] Engineering Tomography Laboratory (ETL), Department of Electronic and Electrical Electrical Engineering, University of Bath, Bath, UK
[c] Nuclear Science and Technology Research Institute, Radiation Safety, Tehran, Iran
[d] Department of Ray Medical Engineering, Shiraz University, Shiraz, Iran

Corresponding author: Ashkan Javaherian
Email address: ashkan.javaherian@yahoo.com
Tel: +49(0) 7720 307 4390
Fax: +49(0) 7720 307 4210

Abstract

Existing total variation (TV) solvers that have been applied in Electrical Impedance Tomography (EIT) smooth the TV function in order to cope with its non-differentiability around the origin, and thus imposes some numerical errors on the solution. Furthermore, these solvers require storage of Hessian, and are thus very impractical for large-scale computations, especially 3D EIT. These shortcomings were addressed by TV solvers that are based on first-order optimization methods. However, the application of these solvers to EIT remains scarce. In this manuscript, we proposes an accelerated version of a gradient-based TV solver based on Augmented Lagrangian and alternating direction method of multipliers, referred to as TVAL3, and apply it to EIT. The results demonstrate the superiority of the accelerated algorithm over existing TV solvers in EIT with regard to both accuracy and speed.

Keywords: electrical impedance tomography; total variation; variable splitting; alternating direction method of multipliers; TVAL3

1. Introduction

Electrical impedance tomography is an attractive imaging technique which aims at reconstructing conductivity distribution inside an object. This is performed via injecting electrical current successively from two electrodes and reading the induced voltages on the remaining electrodes placed on the surface [1-3]. EIT has attracted much interest in medicine [4-6], as well as industry [7-10] because of its high speed and safety. The recovery of conductivity distribution from surface data is in principle to calculate the coefficient of an elliptical partial differential equation subject to a mixed Dirichlet/Neumann boundary condition [11]. The relationship between conductivity field and measured data is very nonlinear. To linearize the problem, Jacobian is computed, which is severely ill-conditioned. To mitigate this ill-posedness, *a priori* assumption about the conductivity, e.g., smoothness or sparsity, is imposed [12-14].

Quadratic regularization often deteriorates the spatial resolution via smoothing the reconstructed image [12,15], whereas sparsity regularization has demonstrated its great potential in recovering sparse signals/images [16-17]. In many cases, a sequence of expansion coefficients of the signal over an orthonormal basis includes only a small number of nonzero entries, and is thus assumed sparse [11,17]. In many applications in EIT, the object under study involves an uninteresting background plus a number of interesting inclusions, which represents sparsity [11,18-21].

However, it turns out that total variation regularization better preserves inter-medium discontinuities than the sparsity regularization. The literature in the context of signal/image processing has shown the superiority of the TV minimization over the sparsity in reconstructing staircase signals or piecewise constant images, as the TV function represents the sparsity of gradient [22]. In EIT the TV minimization was employed to detect sharp transitions over piecewise constant conductivity fields [23].

Another strategy for determining sharp interfaces over piecewise fields is Level Set (LS) method [24-25]. However, so far it has not demonstrated its potential in practical EIT since the level set function increases the ill-posedness of the problem because of null space of the arising forward operator [26-28]. Indeed, LS functions are typically meaningful solely around the zero level.

TV minimization dates back to 1992, when Rudin-Osher-Fatemi (ROF) scheme was introduced in order for denoising problem to recover sharp interfaces in images [29]. Since then, many studies were done in order to improve TV optimization [30-38]. The main problem was the non-differentiability of the TV function around the origin, which was often addressed by smoothing this function [23,30,36]. Newton-based methods are often employed in order to minimize the smooth TV function. The convergence properties of Newton's method in TV minimzation were reported by Chan et al [32] and Vogel [38].

To the best of our knowledge, Lagged Diffusivity (LD) [33,35] and Primal-Dual Interior-Point-Method (PD-IPM) [34] are the most efficient TV codes that were employed in EIT [39], and are now available on the EIDORS website [40]. Borsic et al [39] showed the superiority of the PD-IPM method over the LD method in preserving sharp discontinuities. However, these algorithms are based on second-order optimality condition, and thus require the inverse Hessian. In practice, the Hessian is not computationally inverted, but leads to a system of linear equations, which is still costly in large-scale problems [39]. As a result, these second-order solvers are very expensive for medical applications where very high spatial resolution is demanded, together with a fast reconstruction.

Considering accuracy, continuation strategies were suggested to mitigate errors arising from smoothing the TV functional, but this error still imposes some numerical errors to the solution [13,32].

In the sequel, the recent advances on TV minimization are overviewed. The TV minimization was formulated as a Second Order Cone Programming (SOCP), which was solved by an interior-point method [41]. However, the convergence of SOCP has not been established for high dimensional problems. Applying l_1-magic to SOCP, Newton's method is applied in a recursive way rather than directly solving the linear system [42-44]. Nevertheless, these algorithms are still time consuming because of applying the Newton's method. Relying on the well-known Iterative Shrinkage/Thresholding (IST) technique, an alternating minimization algorithm that involves two-steps of IST, referred to as Two-Step IST (TWIST), was proposed [45-46]. Chambolle proposed an iterative fixed-point TV scheme based on the well-known dual approach and TWIST [47]. Later, a modified variant of Nesterov's

algorithm, referred to as NESTA, was developed to minimize saddle-point problems over constrained convex sets [49].

Grounded on applying alternating minimization algorithm to the so-called half quadratic problem, a new TV minimization scheme based on variable-splitting technique was proposed [50]. The per-iteration computation involves, alternatively, a shrinkage formula to minimize the objective function with respect to a slack variable handling the non-differentiability of the TV function as well as three fast Fourier transforms (FFTs) to minimize the function with respect to the sought gray-level image (cf. section 2.4). It removes the costly Newton's method, but it requires the multipliers to reach infinity in order to ensure the convergence of the algorithm. This, in turn, increases the ill-posedness of the problem [50-51].

To overcome these shortcomings, a robust gradient-based TV algorithm based on Augmented Lagrangian and Alternating direction method of multipliers, referred to as TVAL3, was proposed [51]. This involves two sub-problems per iteration, the first of which is to minimize an augmented Lagrangian function with respect to the mentioned slack variable, and the second is to minimize the objective function roughly with respect to the sought gray-level image by a one-step gradient descent scheme [51].

In contrast with a great deal of sparsity regularization schemes that have been applied to EIT [16-21], the recent advances on TV minimization have not been paid due attention. As far as we know, TVAL3 is the most powerful TV algorithm in the context of image restoration [51-52]. On the other hand, PD-IPM is known to be the most efficient TV algorithm in EIT [39], and is available on the EIDORS website [40-a]. In this study, the TVAL3 solver is accelerated by the so-called Fast Iterative Shrinkage-Thresholding Algorithm (FISTA), and then the performance of the resulting scheme is investigated in EIT. The accelerated TVAL3 is specifically tailored to EIT so that it matches the underlying finite element domain rather than gray-level images via locally weighting the TV function proportionally to length of edges between finite elements. The optimality criteria are changed in conformity with our special purpose. The results indicate the superiority of the accelerated TVAL3 to the standard TVAL3 with respect to speed, and to the PD-IPM algorithm with regard to both accuracy and speed.

2. Theory

2.1. Forward and inverse models

Given a bounded Lipschitz domain $\Omega \in R^d \, (d=2,3)$, and the Sobolev space $H^1(\Omega)$, $\tilde{H}^1(\Omega)$ is a subspace of $H^1(\Omega)$, i.e.,

$$\tilde{H}^1(\Omega) = \left\{ \upsilon \in H^1(\Omega) \, : \, \int_{\partial\Omega} \upsilon ds = 0 \right\}. \tag{1}$$

By neglecting magnetic induction, the Maxwell's laws are described by the following partial differential equation [11]. Find $u \in \tilde{H}^1(\Omega)$ such that

$$\begin{aligned} -\nabla.(\sigma \nabla u) &= 0 && in \ \ \Omega \\ \sigma \partial u / \partial n &= j && on \ \ \partial\Omega \end{aligned}. \tag{2}$$

Solving Eq. (2), the injected current j is linearly linked to the induced electrical potential u on the boundary by a map called Neumann to Dirichlet, which is written as

$$\begin{aligned} \Lambda_\sigma : L^2(\partial\Omega) &\to L^2(\partial\Omega) \\ j &\to u|_{\partial\Omega} \end{aligned}, \tag{3}$$

where $L^2(\partial\Omega)$ denotes the boundary $\partial\Omega$ in L^2 space. The NtD map is nonlinear with respect to σ, so it is linearized by computing the Jacobian around σ_0. This gives a map that is a linear function of both σ and j in the form

$$D\Lambda(\sigma)j = u\big|_{\partial\Omega} \tag{4}$$

From a practical point of view, to deal with errors occurring during the measurement process, difference imaging is often preferred to static imaging [3]. Conversely, the calculation of σ from u cannot be done straightforwardly by inversion of the linearized map since a noisy version $D\Lambda_{\tilde{\sigma}} \in L^2(\partial\Omega)$ of the linear NtD map $D\Lambda(\sigma) \in L^2(\partial\Omega)$ is measured in practice. Instead, the solution will be the minimizer of discrepancy functional in the form

$$\min_{\sigma \in A}\left\|D\Lambda(\sigma) - D\Lambda_{\tilde{\sigma}}\right\|_{L^2(\partial\Omega)}, \tag{5a}$$

where *A* is an admissible set of the conductivity distribution.

From a practical point of view, the reconstruction of σ from u is subject to errors during the measurement process, e.g., electrode movements. As a result, difference imaging is often preferred to absolute imaging [3]. Accordingly, one seeks the difference of conductivity distribution between two frames of data taken at times t_1 and t_2 from electrical potentials $u(t_1)$ and $u(t_2)$. Accordingly, the discrepancy functional is recast in the form

$$\min_{\delta\sigma \in A}\left\|D\Lambda(\delta\sigma) - D\Lambda_{\delta\tilde{\sigma}}\right\|_{L^2(\partial\Omega)}, \tag{5b}$$

The linearized map given in Eq. (4) is severely ill-conditioned. To see a proof on the ill-conditioning of the map, the reader is referred to [11]. To combat this ill-conditioning, the solution is constrained by *a priori* assumption about the conductivity field, e.g., smoothness or sparsity. Accordingly, the solution will be the minimizer of the following objective functional

$$\min_{\delta\sigma \in A}\frac{1}{2}\left\|D\Lambda(\delta\sigma) - D\Lambda_{\delta\tilde{\sigma}}\right\|_{L^2(\partial\Omega)} + \lambda\left\|\delta\sigma\right\|_{\ell^r}^r \qquad 1 \le r \le 2. \tag{6}$$

The choice $r = 2$ raises the classical smoothness penalty, while the choice $r \in [1,2)$ enforces sparsity [11]. The sparsity imposes more vigorous constraint than the smoothness since $\ell^r (r \in (1,2))$ is a subspace of ℓ^2 [11]. Although sparsity penalties have demonstrated their great potential in recovering sparse conductivity fields, e.g., anomalies with a simple mathematical description, it cannot recover precisely sharp transitions over large-scale piecewise conductivity fields when the gradient of the conductivity field rather than the conductivity itself is sparse.

2.2. Total variation functional

To preserve sharp edges over the conductivity field, one initially assumes that the unknown conductivity $\delta\sigma$ is piecewise constant. To attain this objective, the sum of the spatial gradient of the conductivity, the so-called Total Variation (TV), i.e.,

$$TV(\delta\sigma) = \int_{\Omega}\left|\nabla(\delta\sigma)\right|, \tag{7}$$

is minimized as follows.

Assume $BV(\Omega)$ be a space of functions in Ω with a bounded variation, which satisfies

$$\left\|\delta\sigma\right\|_{BV(\Omega)} = \left\|\delta\sigma\right\|_{L^1(\Omega)} + \int_{\Omega}\left|\nabla\delta\sigma\right|. \tag{8}$$

Accordingly, the solution is expected to be the minimizer of the TV function subject to the constraint $D\Lambda(\delta\sigma) = D\Lambda_{\delta\tilde{\sigma}}$, which is written as

$$\min_{\delta\sigma \in X} \int_{\Omega} |\nabla\delta\sigma| \qquad \text{s.t.} \qquad D\Lambda(\delta\sigma) = D\Lambda_{\delta\tilde{\sigma}}, \tag{9}$$

where $X = \{\delta\sigma \in BV(\Omega) : \delta\sigma|_{\partial\Omega} = 0\}$.

The exact solution of $\nabla(\delta\sigma)$ is not computationally tractable because of the ill-posedness of the problem. Instead, a blurred version $\nabla(\delta\tilde{\sigma}) = \nabla(\delta\sigma + \eta)$ is calculated in practice instead, which satisfies

$$\int_{\Omega} |\nabla(\delta\sigma + \eta)| \geq \int_{\Omega} |\nabla\delta\sigma|. \tag{10}$$

The unconstrained variant of the problem is formed by penalizing the constraint, which yields the following augmented functional.

$$\min_{\delta\sigma \in X} \int_{\Omega} |\nabla\delta\sigma| + \frac{\alpha}{2} \|D\Lambda(\delta\sigma) - D\Lambda_{\delta\tilde{\sigma}}\|_2^2 \tag{11}$$

The resulting problem is now expressed in a discrete form. The finite element approximation u^h of electrical potential u over a finite element domain of size N_n can be described as an expansion of N_n characteristic functions in the form

$$u = \sum_{k=1}^{N_n} a_k \varphi_k(x), \qquad x \in \Omega. \tag{12}$$

Where, $\varphi_k(x)$ and a_k respectively, represent basis function k at point $x \in \Omega$ and its associated coefficient. The conductivity distribution is now represented over N_s finite elements, and is linearly linked to the electrical potential on electrodes by the Jacobian $J \in R^{M \times N_s}$, where M is the number of measurements between the electrodes.

To define the TV penalty, the spatial gradient matrix must be computed. To compute the gradient between two neighboring finite elements which share edge i, $\nabla(\delta\sigma)$ is set to zero over the entire domain except on that edge. Consequently, over a mesh made up of N_e edges and N_s elements, the gradient matrix $G \in R^{N_e \times N_s}$ is a sparse matrix where each row has two nonzero entries on indices sharing the corresponding edge, and is zero elsewhere. For instance, the row $G_i = [0,...,0, g_i,...,-g_i,0,...,0]$ pertaining to edge i takes two nonzero values on the indices sharing this edge, and is zero elsewhere. g_i is the length of edge i, and its sign denotes the two sides of this edge. The minimizer is thus rewritten as

$$\min_{\delta\sigma} \sum_{i=1}^{N_e} |G_i \delta\sigma| + \frac{\alpha}{2} \|J\delta\sigma - \delta V\|_2^2. \tag{13}$$

Where, δV is the difference between two frames of data, and $\sum_{i=1}^{N_e} |G_i \delta\sigma|$ represents the discrete total variation $TV(\delta\sigma)$. To combat the non-differentiability of the TV functional in the neighborhood of zero, $TV(\delta\sigma)$ is smoothed around the origin, which yields

$$TV_\theta(\delta\sigma) = \sqrt{|TV(\delta\sigma)|^2 + \theta}, \tag{14}$$

where θ is the smoothing parameter.

2.3. Primal-Dual Interior-Point-Method

To the best of our knowledge, the most efficient TV solver that has been employed in EIT is the Primal-Dual Interior-Point-Method (PD-IPM). It was demonstrated that the PD-IPM is the most accurate algorithm among TV solvers that are based on second-order optimization techniques [39]. This solver is freely available on EIDORS website, which was used in this study [40]. Applying the PD-IPM, the problem involves two objective functions, Primal (P) and Dual (D), in the form [39]

$$P(\delta\sigma) = \min_{\delta\sigma} \frac{1}{2}\|J\delta\sigma - \delta V\|_2^2 + \lambda\sum_i |G_i\delta\sigma| \tag{15a}$$

$$D(\delta\sigma) = \max_{\chi:|\chi_i|\leq 1}\min_{\delta\sigma} \frac{1}{2}\|J\delta\sigma - \delta V\|_2^2 + \lambda\sum_i \chi_i G_i\delta\sigma \tag{15b}$$

where $\lambda \equiv 1/\alpha$, and χ denotes the vector of auxiliary variables, the so-called dual variables. The optimal solution is the point where the difference between these two functions, namely Primal-Dual gap, becomes zero [39]. This condition is called *Complementarity* condition, and is derived in the form

$$\left(|G_i\delta\sigma| - \chi_i|G_i\delta\sigma|\right) = 0, \qquad i = 1,...,N_e. \tag{16}$$

Gauss-Newton algorithm is applied to iteratively reach the complementary condition, which gives updated formulas [39]

$$\delta\sigma_{k+1} = -[J_k^T J_k + \lambda G^T E_k^{-1} F_k G]^{-1}[J_k^T(J\delta\sigma_k - \delta V) + \lambda G^T E_k^{-1}G\delta\sigma_k] + \delta\sigma_k \tag{17a}$$

$$\chi_{k+1} = \mathbf{E}_k^{-1}G\delta\sigma_k + \mathbf{E}_k\mathbf{F}_kG(\delta\sigma_{k+1} - \delta\sigma_k) \tag{17b}$$

Where,

$$E_k = \operatorname{diag}\left(\sqrt{|G_i\delta\sigma_k|^2 + \theta}\right) \tag{18a}$$

$$F_k = \operatorname{diag}\left(1 - \frac{\chi_{(i,k)}G_i\delta\sigma_k}{\sqrt{|G_i\delta\sigma_k|^2 + \theta}}\right). \tag{18b}$$

The stopping criterion of the PD-IPM solver was considered as

$$\frac{\|\delta\sigma^{k+1} - \delta\sigma^k\|}{\|\delta\sigma^k\|} < 1\times 10^{-3}. \tag{19}$$

2.4. Alternating Direction Method of Multipliers (ADMM)

Smoothing the TV functional around the origin typically imposes some numerical errors on the solution, and deleteriously affects the convergence. To address this issue, continuation strategies were proposed on the choice of θ, which slightly reduce the errors arising from the smoothing parameter [13,32].

To evade this smoothing action, Wang et al [50] proposed a variable-splitting scheme. This approach uses a slack variable at each image pixel, which shifts the gradient out of the non-differentiable region, and then penalizes this deviation at that pixel. In this work, we modify the TVAL3 code available in [52] so that it matches the underlying finite element domain, and then combine it with Fast Iterative Shrinkage Thresholding Algorithm (FISTA) [54] in order to considerably enhance its speed.

Over a finite element domain, the slack variable can be described on each edge as a scalar variable $\omega_i \in R$ $(i = 1,...,N_e)$ which represents the differentiable variant of the gradient of the conductivity changes on that edge. The total variation of the defined

slack variable is thus differentiable around the origin. The resulting problem is of the form [51]

$$\min_{\omega} \sum_i \|\omega_i\| \qquad \text{s.t.} \qquad J\delta\sigma = \delta V \quad \text{and} \quad G_i\delta\sigma = \omega_i, \ i = 1,...,N_e. \tag{20}$$

Penalizing the constraint on data as a quadratic penalty and the constraint on the slack variable as an element-wise quadratic norm yields the unconstrained variant of the problem, the so-called *half-quadratic* problem, i.e.,

$$\min_{\omega,\delta\sigma} \ \phi(w_i,\delta\sigma) := \sum_i (\|\omega_i\| + \frac{\beta}{2}\|G_i\delta\sigma - \omega_i\|_2^2) + \frac{\alpha}{2}\|J\delta\sigma - \delta V\|_2^2. \tag{21}$$

At each iterate, the objective function is first minimized with respect to ω_i by the shrinkage formula in the form

$$\omega_{(i,k+1)} = \max\left\{|G_i\delta\sigma_k| - \frac{1}{\beta}, 0\right\}\text{sgn}(G_i\delta\sigma_k). \tag{22}$$

The objective function is now a function of the updated slack variable in the form as

$$\phi(\omega_{(i,k+1)},\delta\sigma) = \sum_i (\|\omega_{i,k+1}\| + \frac{\beta}{2}\|G_i\delta\sigma - \omega_{i,k+1}\|_2^2) + \frac{\alpha}{2}\|J\delta\sigma - \delta V\|_2^2. \tag{23}$$

Nulling the gradient of the updated objective function with respect to $\delta\sigma$ yields

$$\delta\sigma_{k+1} = (\sum_i G_i^T G_i + \frac{\alpha}{\beta} J^T J)^+ (\sum_i G_i^T \omega_{i,k+1} + \frac{\alpha}{\beta} J^T \delta V), \tag{24}$$

where $+$ stands for Moore-Penrose pseudo inverse of the underlying matrix, the so-called Hessian $H \in R^{N_s \times N_s}$. Typically, the major cost of solving Eq. (24) is the inverse Hessian, which is not computationally tractable in large-scale problems. Instead, an equivalent linear system of equations is solved iteratively by least square methods, which is still very expensive. In addition, the storage of the Hessian matrix for large-scale problems is often impractical.

Another shortcoming is the multiplier β which must go to infinity by the progression of the algorithm in order to guarantee that the solution of Eq. (21) converges to that of Eq. (13). Unfortunately, the large values of β considerably increase the ill-condition of the problem, though adopting continuation approaches mitigates this ill-posedness to some degree [50].

To address these difficulties, a TV minimization approach based on augmented Lagrangian function was proposed. The key point of the algorithm is to penalize each constraint as an augmented Lagrangian function rather than a quadratic norm, which gives [51]

$$\begin{aligned}\psi(\omega_i,\delta\sigma) = &\sum_i (\|\omega_i\| - \rho_i^T (G_i\delta\sigma - \omega_i) + \frac{\beta_i}{2}\|G_i\delta\sigma - \omega_i\|_2^2) \\ &- \zeta^T (J\delta\sigma - \delta V) + \frac{\alpha}{2}\|J\delta\sigma - \delta V\|_2^2 \end{aligned}. \tag{25}$$

The minimization of the above functional involves some outer iterations denoted by superscript k and inner iterations labeled by subscript k. At every iteration the multipliers ρ_i and ζ are first updated in the form

$$\rho_i^k = \rho_i^{k-1} - \beta_i(G_i\delta\sigma^k - \omega_i^k) \qquad \text{for all } i \tag{26a}$$

$$\zeta^k = \zeta^{k-1} - \alpha(J\delta\sigma^k - \delta V). \tag{26b}$$

Here the initial values are set to $\rho_i^0, \zeta^0 = 0$. Analogous to the half-quadratic problem, the first sub-problem is to minimize the objective function with respect to ω_i on each edge in the form

$$\min_{\omega_i} \sum_i (\|\omega_i\| - \rho_i^T (G_i \delta\sigma - \omega_i) + \frac{\beta_i}{2} \|G_i \delta\sigma - \omega_i\|_2^2) . \tag{27}$$

This is done by a shrinkage-like formula in the form

$$\omega_{(i,k+1)} = \max\left\{\left|G_i \delta\sigma_k - \frac{\rho_i}{\beta_i}\right| - \frac{1}{\beta_i}, 0\right\} \operatorname{sgn}(G_i \delta\sigma_k - \frac{\rho_i}{\beta_i}) \tag{28}$$

Having $\omega_{i,k+1}$ at hand, the second sub-problem is to minimize the objective function with respect to $\delta\sigma$ [51], i.e.,

$$\min_{\delta\sigma} \quad \psi(\omega_{(i,k+1)}, \delta\sigma) = \sum_i (\|\omega_{(i,k+1)}\| - \rho_i^T (G_i \delta\sigma - \omega_{(i,k+1)}) + \frac{\beta_i}{2}\|G_i \delta\sigma - \omega_{(i,k+1)}\|_2^2)$$
$$- \zeta^T (J\delta\sigma - \delta V) + \frac{\alpha}{2}\|J\delta\sigma - \delta V\|_2^2 \tag{29}$$

The exact minimizer of the above sub-problem is calculated by differentiating the objective function with respect to $\delta\sigma$, which yields

$$\frac{d\psi(\omega_{(i,k+1)}, \delta\sigma_k)}{d\delta\sigma} = \sum_i (\beta_i G_i^T (G_i \delta\sigma_k - \omega_{(i,k+1)}) - G_i^T \rho_i)$$
$$+ \alpha J^T (J\delta\sigma_k - \delta V) - J^T \zeta \tag{30}$$

Enforcing $d\psi(\omega_{(i,k+1)}, \delta\sigma_k)/d\delta\sigma = 0$ yields

$$\delta\sigma_{k+1} = [\sum_i \beta_i G_i^T G_i + \alpha J^T J]^+ [\sum_i (G_i^T \rho_i + \beta_i G_i^T \omega_{(i,k+1)}) + J^T \zeta + \alpha J^T \delta V] \tag{31}$$

As discussed above, the calculation of the Moore-Penrose pseudo inverse considerably increases the computational cost. Instead, the steepest descent method is employed to recursively solve $\delta\sigma$ at each iteration in the form

$$\delta\tilde{\sigma} = \delta\sigma - \gamma \frac{d\psi}{d\delta\sigma} . \tag{32}$$

Each recur requires computation of the gradient in Eq. (30), which is computationally costly. So a single step of the steepest descent method is often implemented at each outer iteration to compute a rough approximation of $\delta\sigma_{k+1}$, i.e.,

$$\delta\tilde{\sigma}_{k+1} = \delta\sigma_k - \tilde{\gamma}_k \frac{d\psi(\omega_{(i,k+1)}, \delta\sigma_k)}{d\delta\sigma} \tag{33}$$

The step length $\tilde{\gamma}_k$ is estimated by Barzilai-Borwein (BB) method [51-53]. $\delta\sigma_{k-1}$ and $\delta\sigma_k$ from two previous iterations are utilized to estimate the step length as follows. Having defined

$$s_k = \delta\sigma_k - \delta\sigma_{k-1} \tag{34a}$$

$$g_k = \frac{d\psi(\omega_{(i,k+1)}, \delta\sigma_k)}{d\delta\sigma} - \frac{d\psi(\omega_{(i,k+1)}, \delta\sigma_{k-1})}{d\delta\sigma}, \tag{34b}$$

an initial guess of the step length is calculated as follows.

$$\gamma_k = \frac{s_k^T s_k}{s_k^T g_k} . \tag{35}$$

Considering γ_k as the first guess, the convergence of the algorithm is checked through the following loop until the following Nonmonotone Armijo condition is satisfied.

Nonmonotone Armijo loop
$\quad$ While $\quad \psi(\omega_{(i,k+1)}, (\delta\sigma_k - \gamma_k (d\psi_k / d\delta\sigma))) \geq (M_k - \vartheta\gamma_k (d\psi_k / d\delta\sigma)^T d\psi_k / d\delta\sigma)$
$\qquad \gamma_k = \varepsilon\gamma_k$

End

Where, $d\psi_k / d\delta\sigma = \dfrac{d\psi(\omega_{(i,k+1)}, \delta\sigma_k)}{d\delta\sigma}$, and M_k is calculated as follows.

$$Q_k = \eta Q_{k-1} + 1 \tag{36a}$$

$$M_k = (\eta Q_{k-1} M_{k-1} + \psi(\delta\sigma_k))/Q_k \tag{36b}$$

and $0 < \eta < 1, 0 < \varepsilon < 1$ are scalar values.

Here η and ε are set close to 1 for iterates far from the optimum, i.e., $\eta_0, \varepsilon_0 = 0.995$, and are set close to zero for iterates close to the optimum. β_i is assumed fixed over all edges in the finite element domain, and ϑ is empirically set to $\vartheta = 10^{-5}\beta$.

The algorithm is now accelerated based on FISTA method [54]. To attain this aim, a linear combination of $\delta\sigma^{k+1}$ and $\delta\sigma^k$ is used to update the iterate as follows.

$$t^{k+1} = \frac{1 + \sqrt{1 + 4(t^k)^2}}{2} \tag{37a}$$

$$y^{k+1} = \delta\sigma^{k+1} + \frac{t^k - 1}{t^{k+1}}(\delta\sigma^{k+1} - \delta\sigma^k), \tag{37b}$$

which is initialized by $y^0 = \delta\sigma^0 = 0$ and $t^1 = 1$. We restart iterates of FISTA by $t^k = 1$ whenever $\psi(w_i^{k+1}, \delta\sigma^{k+1}) \geq \psi(w_i^k, \delta\sigma^k)$ in order to avoid any increase in the objective function since applying FISTA, the objective function is typically prone to an unwanted oscillation with the progression of iterates.

In what follows, the proposed accelerated TVAL3 algorithm is overviewed at a glance. The stopping criterion of the algorithm is enforced similarly to that of the PD-IPM in order to make a fair comparison between the competing solvers.

<u>Algorithm 1.</u>   **Initialize:** $\omega_i^0 = y^0 = \delta\sigma^0 = \zeta^0 = 0, \rho_i^0 = 0 \ \ (i = 1, ..., N_e)$, $t^1 = 1$
 	
 Set β, α , $\vartheta = 10^{-5}\beta$
 	
      Outer loop: While $\dfrac{\left\| \delta\sigma^{k+1} - \delta\sigma^k \right\|}{\left\| \delta\sigma^k \right\|} \geq 1 \times 10^{-3}$
 	
          Initialize $\eta_0, \varepsilon_0 = 0.995,$
          $\delta\sigma_0^{k+1} = y^k, \ \omega_{(i,0)}^{k+1} = \omega_i^k$
          $M_0 = \psi(\omega_{(i,0)}^{k+1}, \delta\sigma_0^{k+1})$
 	
      Inner loop: While $\left\| \dfrac{\psi(\omega_{(i,k)}^{k+1}, \delta\sigma_k^{k+1})}{\psi(\omega_{(i,k-1)}^{k+1}, \delta\sigma_{k-1}^{k+1})} - 1 \right\| \geq 1 \times 10^{-2}$
 	
          Update $\omega_{(i,k+1)}^{k+1}$ by shrinkage formula
          Estimate γ_k by *BB* scheme
          Calculate $\tilde{\gamma}_k$ by Non-monotone Armijo loop
          Update $\delta\sigma_{k+1}^{k+1}$ by steepest descent meh
          Calculate $M_{k+1} = \psi(\omega_{(i,k+1)}^{k+1}, \delta\sigma_{k+1}^{k+1})$
     End Inner loop
          Set $\delta\sigma^{k+1} = \delta\sigma_{k+1}^{k+1}, \ \omega_i^{k+1} = \omega_{(i,k+1)}^{k+1}$
      If $\psi(w_i^{k+1}, \delta\sigma^{k+1}) < \psi(w_i^k, \delta\sigma^k)$

$$t^{k+1} = \frac{1 + \sqrt{1 + 4(t^k)^2}}{2}$$

Else

$$t^k = 1, \ t^{k+1} = 1$$

End If

$$y^{k+1} = \delta\sigma^{k+1} + \frac{t^k - 1}{t^{k+1}}(\delta\sigma^{k+1} - \delta\sigma^k)$$

Update ρ_i^k, ζ^k

End While

End Outer loop

3. Numerical results

The processor that was used in this work is an Intel(R) Core(TM) i5-4570 CPU @ 3.20 GHz with a RAM of 8.00 GB and a 64-bit operating system (Windows 7, Microsoft).

3.1. 2D simulated phantom

The PD-IPM method was considered as a benchmark in our study, as it is the most accurate TV solver employed in EIT. The 2D phantom was simulated analogously to that presented in Borsic et al [39]. The FEM model was made up of 1600 triangular elements. The background conductivity was set to $1 \, Sm^{-1}$, and two anomalies having the conductivities of $0.5 \, Sm^{-1}$ and $1.5 \, Sm^{-1}$ provide a narrow gap, making a challenge for reconstruction. The simulated conductivity distribution has sharp interfaces. Sixteen electrodes were evenly placed around the surface based on complete electrode model with a contact impedance of $10 \, \Omega m$, and the measurements were done according to the well-known adjacent strategy. An electrical current with amplitude of 10 mA was successively injected through each pair of adjacent electrodes, and the induced voltages were measured between the remaining pairs of adjacent electrodes. In total, 104 voltages were measured. The phantom is shown in Fig. 1. Additive White Gaussian Noise (AWGN) with different levels of noise was incorporated to data, i.e.,

$$Noise = NL \cdot \mathrm{std}(\delta V) \cdot ND. \tag{38}$$

Where, NL is the noise level, $\mathrm{std}(\delta V)$ is the standard deviation of the difference measured data, and ND is a vector-valued standard normal distribution.
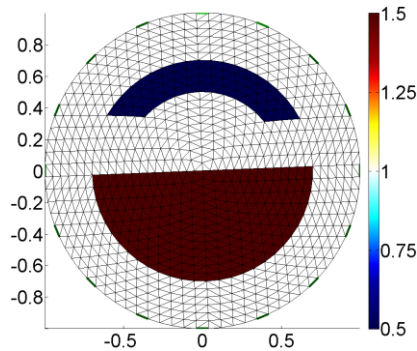

Fig. 1. The 2D simulated phantom, similar to that used in Borsic et al [39].

The inverse solvers were applied to a mesh made up of 1024 elements in order to avoid inverse crime. Employing the PD-IPM solver, the images were successfully reconstructed over an extensive range of the regularization parameters, i.e., $10^{-3} \leq \lambda \leq 10^{-1}$ so that 11 values are placed equidistantly on a logarithmic scale. On the other hand, employing the modified TVAL3 solver, the inverse of the multipliers α and β are presented since $1/\alpha$ in the TVAL3 is equal to λ in the PD-IPM, comparing Eq. (13) with Eq. (15-a). The range of $1/\alpha$ was chosen similarly to λ. For simplicity, β_i values were fixed over the entire domain. To reconstruct images, the solvers were terminated when the optimality criteria are satisfied (c.f. section 2). The accuracy of each reconstructed image was calculated with respect to Relative Error (RE), i.e.,

$$RE = \frac{\left\| \delta\sigma_{reconstructed} - \delta\sigma_{true} \right\|}{\left\| \delta\sigma_{true} \right\|} . \tag{39}$$

Figs. 2(a-d) respectively, exhibit RE of images reconstructed from data incorporated with 1%, 3%, 5% and 10% noise levels against the chosen regularization parameters. As shown in Fig (2), three values of $1/\beta$, 2e-3, 1e-3 and 8e-4, were chosen to demonstrate the performance of TVAL3. As shown in this Figure, the RE values were successfully reduced by the accelerated TVAL3 relative to the PD-IPM for all chosen values of α and β.
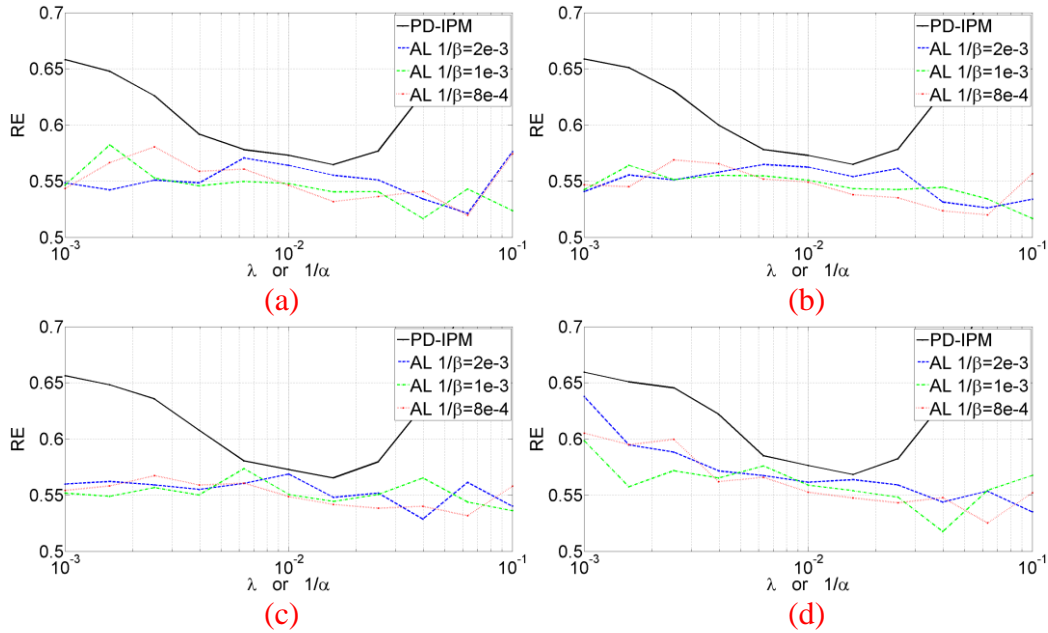

Fig. 2. Relative Error of the reconstructed images of the 2D simulated phantom against the regularization parameter $\lambda \equiv 1/\alpha$. The data were incorporated with AWGN with noise levels: (a) 1%, (b) 3%, (c) 5%, (d) 10%.

Table 1 shows the optimal images of the curves shown in Fig. 2. The optimal regularization parameter associated with each curve was considered the point that produced the minimal RE on that curve. From this table, the accelerated TVAL3 algorithm produced the optimal images with a lower RE than the PD-IPM for all noise levels. The optimal images reconstructed by the accelerated TVAL3 solver from the noisy data corrupted with a 10% noise level are more accurate than the optimal image obtained by PD-IPM from the data corrupted with only a 1% noise level.

Noise Level	Regularization parameter	PD-IPM		Accelerated TVAL3		
				$1/\beta = 2e-3$	$1/\beta = 1e-3$	$1/\beta = 8e-4$
1%	$\lambda \equiv 1/\alpha$	1.58e-2		6.31e-2	3.98e-2	6.31e-2
	RE	5.646 e-1		5.214e-1	5.166e-1	5.196e-1
3%	$\lambda \equiv 1/\alpha$	1.58e-2		6.31e-2	1e-1	6.31e-2
	RE	5.648e-1		5.261e-1	5.167e-1	5.199e-1
5%	$\lambda \equiv 1/\alpha$	1.58e-2		3.98e-2	1e-1	6.31e-2
	RE	5.654e-1		5.287e-1	5.362e-1	5.318e-1
10%	$\lambda \equiv 1/\alpha$	1.58e-2		1e-1	3.98e-2	6.31e-2
	RE	5.683e-1		5.351 e-1	5.176e-1	5.252e-1

Table 1. The optimal images obtained from the 2D simulated phantom.

Figs. 3(a) and (b) show the images reconstructed by the PD-IPM solver with the optimal regularization parameter from noisy data with noise levels of 5% and 10%, respectively. The images were obtained when the stopping criterion was satisfied.

Figs. 4(a) and (b) show the images reconstructed by the accelerated TVAL3 with the optimal regularization parameter and $\beta = 8e-4$ from noisy data with noise levels of 5% and 10%, respectively. Figs. 3(a) and (b) indicate that the PD-IPM produced a slightly sharper image than the accelerated TVAL3, but it determined the interfaces with a low accuracy. It is observed that the inter-medium boundaries have been recovered falsely, relative to the phantom in Fig. (1). Indeed, the sharpness of an image is efficient as long as the accuracy holds. Figs. 3(c) and (d) show that the modified TVAL3 solver has recovered the discontinuities more accurately than the PD-IPM, and produced a smaller artifact.
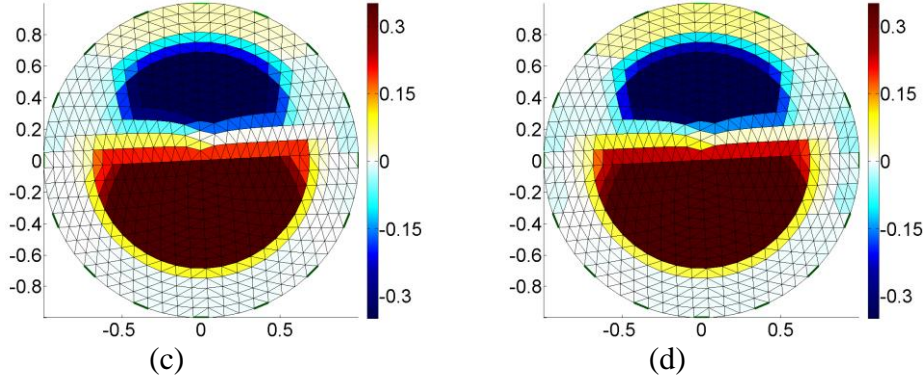

(a)   (b)

(c)	(d)
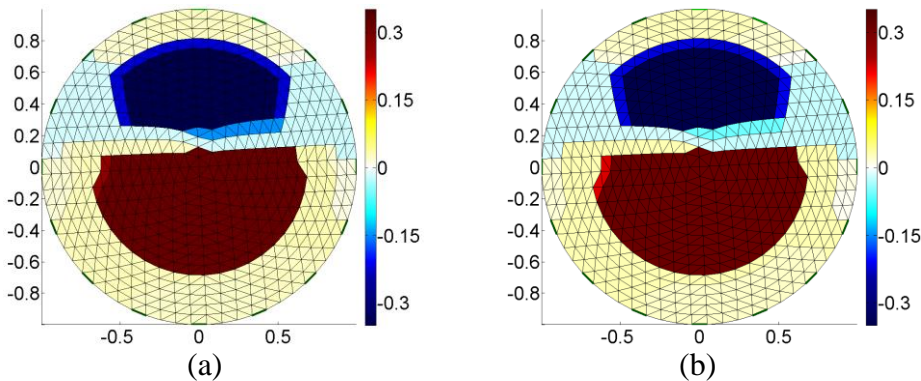
Fig. 3. The optimal image of the 2D simulated phantom, reconstructed by PD-IPM from data with noise levels: (a) 5%, and (b) 10%, and the optimal image reconstructed by accelerated TVAL3 with $1/\beta = 8e-4$ from data with noise levels: (c) 5%, and (d) 10%.

As discussed in sections 1 and 2, the main advantage of TVAL3 relative to PD-IPM is the computational cost since TVAL3 is performed without the need for the inverse Hessian. Note that in second-order optimization methods like PD-IPM, the Hessian is not computationally inverted, and instead the arising linear system of equations is solved recursively by least squares method, but this is still more expensive than gradient-based methods like TVAL3. In this study, TVAL3 was further accelerated relying on FISTA strategy, which was proposed in [54].

Table 2 shows the mean CPU time elapsed for reconstructing an image by PDIPM, standard TVAL3 and accelerated TVAL3. Standard TVAL3 is the algorithm without the acceleration due to FISTA. Considering each noisy data, the CPU times elapsed by the PD-IPM solver were averaged over the 11 chosen regularization parameters λ, whereas the elapsed times for implementation of the TVAL3 solvers were averaged over 33 different joint choices of multipliers α and β. According to this table, the mean CPU time elapsed for recovering an image by the accelerated TVAL3 was almost four times less than that of the standard TVAL3 and thirteen times less than that of the PD-IPM. As discussed in section 2, all solvers were terminated by the same stopping criterion. Note that the images reconstructed by the standard TVAL3 were very similar to those of the accelerated TVAL3 with regard to accuracy and shape of interfaces, and were thus not shown in this work to avoid repetition.

Noise Level		PD-IPM(Sec)		Standard TVAL3 (Sec)		Accelerated TVAL3(Sec)
1%		1. 6711		0. 5156Sec		0.1237
3%		1.6751		0.5238 Sec		0.1258
5%		1.6881		0.5313 Sec		0.1279
10%		1.6934		0.5372 Sec		0.1302

Table 2. The mean CPU time elapsed by PD-IPM, standard TVAL3 and accelerated TVAL3 for reconstructing an image of the 2D simulated phantom.

3.2. 3D simulated phantom

The 3D phantom was created as a cylindrical mesh, 1 in height and radius, made up of 1024 tetrahedral elements. 32 electrodes were installed aligning two rings around the surface based on complete electrode model by assuming a contact impedance of $10\Omega m^2$ per electrode, and data was collected based on the planar

strategy [55]. The electrical current was injected through each pair of the electrodes with amplitude of 10mA. In total, 464 voltages were measured. Two inclusions having conductivities of $1.5\,Sm^{-1}$ and $0.5\,Sm^{-1}$ were simulated, and the background conductivity was set to $1\,Sm^{-1}$. The simulated phantom is shown in Fig. 4(a). The collected data were contaminated by a 5% and 10% AWGN noise.

To avoid inverse crime, the inverse mesh was made up of 828 finite elements. Analogous to the 2D simulation, the PD-IPM and accelerated TVAL3 solvers were implemented over an extensive range of regularization parameters $\lambda \equiv 1/\alpha$, and β was set to 64 in the TVAL3. The optimal images were computed, which are images with the minimal RE at the stopping point of the algorithms. Table 3 evaluates the reconstructed optimal images with regard to Relative Error and reconstruction time. This table confirms that the accelerated TVAL3 outperforms PD-IPM with respect to both accuracy and speed.

Noise level	Regularization parameters	PD-IPM	Accelerated TVAL3 ($\beta = 64$)
5%	$\lambda \equiv 1/\alpha$	1e-3	5e-4
	RE	3.731e-1	2.231e-1
	CPU Time	3.0463Sec	0.2478Sec
10%	$\lambda \equiv 1/\alpha$	5e-3	2e-3
	RE	5.438e-1	3.512e-1
	CPU Time	3.1576Sec	0.2516 sec

Table 3. The optimal images reconstructed by PD-IPM and accelerated TVAL3 from the 3D simulated phantom.

The optimal images are shown in Fig. 4. Figs. 4(b) and (c) were reconstructed from data with noise level of 5%, whereas Figs. 4(d) and (e) correspond to the 10% noise level. Figs. 4(b) and (d) were reconstructed by the PD-IPM, while Figs. 4(c) and (e) were computed by the accelerated TVAL3. The images were taken at the iteration at which the terminating criterion was satisfied. This figure indicates that the modified TVAL3 solver outperformed PD-IPM in recovering shape of the inclusions.
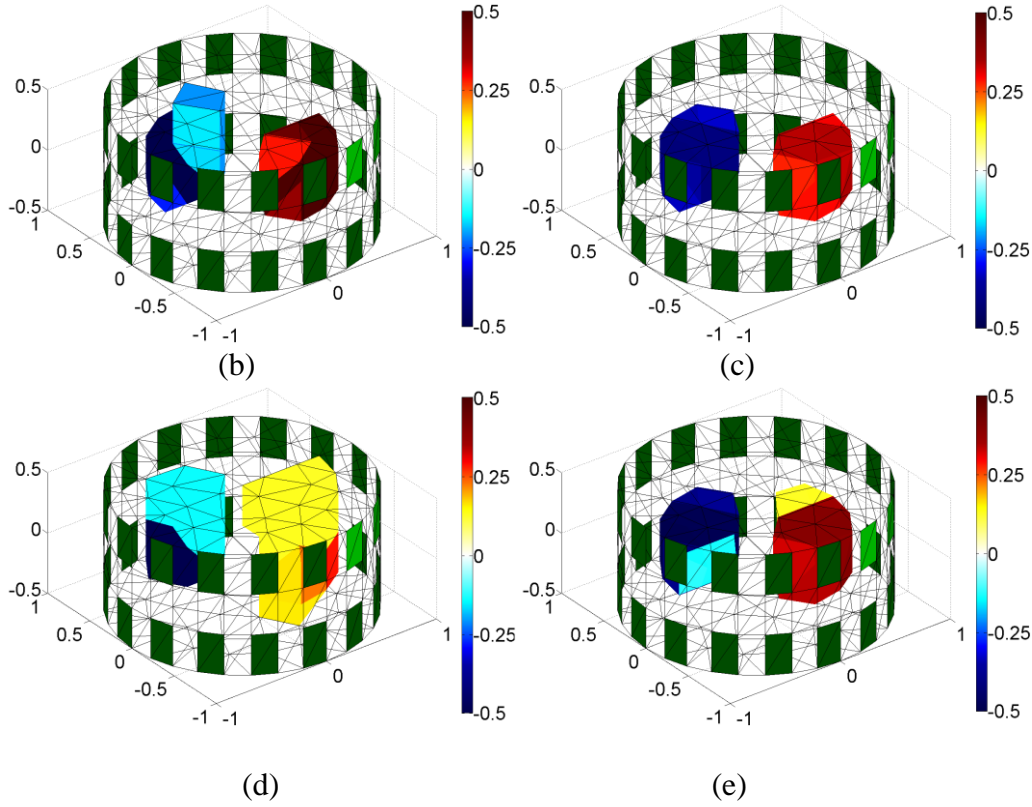

(a)
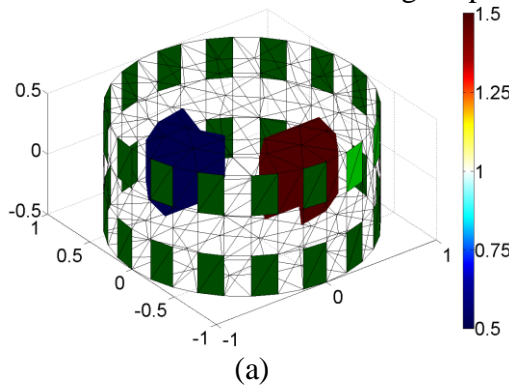
Fig. 4. (a) The 3D simulated phantom. The optimal images reconstructed from data with noise level of 5% by: (b) PD-IPM and (c) accelerated TVAL3, and from data with noise level of 10% by: (d) PD-IPM and (e) accelerated TVAL3.

4. Experimental results

4.1. Imaging of golf balls

To evaluate the performance of the competing solvers in real-world settings, a set of data freely available on the EIDORS website was employed [40-b]. The phantom is a cylindrical pail, 30cm in diameter and height, made of polyethylene, full of 0.9% saline solution. Sixteen electrodes were installed aligning a horizontal ring on the surface of the pail. The inclusions are two non-conductive 2cm radius golf balls. Two setups of this data were utilized, i.e.,

Setup 1- A golf ball was placed at half the radius of the electrode plane.

Setup 2- Two golf balls were placed at half the radius of the electrode plane, one of which was aligning the horizontal axis and the other was aligned by the vertical axis.

The measured data and the Jacobian matrix were normalized in order to cope with the measurement errors. Typically, TV solvers perform well in recovering piecewise conductivity fields having large-scale inclusions, but the recovery of small inclusions is a challenge. Here the merits of the TV solvers in recovering the small golf balls were assessed. The images of the two considered setups were first reconstructed by a one-step quadratic regularized solver, the so-called MAP, where a Gaussian high pass filter was utilized to regularize the solution among an extensive range of the regularization parameters, i.e., 11 values equidistantly placed on a logarithmic scale in the range $10^{-3} \leq \lambda \leq 10^{-1}$. Subsequently, the PD-IPM and the accelerated TVAL3 solvers were applied by 11 multipliers between $10^{-4} \leq \lambda \equiv 1/\alpha \leq 10^{-2}$, and β was set to

15

32 in the TVAL3. Applying each of the solvers, the optimal solution in terms of RE at the iteration that satisfies the stopping criterion was calculated. For measuring RE, the true conductivity field was calculated by matching the area of the golf balls to the FEM model such that the conductivity of the finite elements underlying the interfaces was determined by interpolation. Table 4 presents the merits of the solvers in computing the optimal images. From the measures given in this table, it is observed the modified TVAL3 solver produced smaller RE than the PD-IPM. This table also confirms that the accelerated TVAL3 is almost ten times faster than the PD-IPM.

Setup	Regularization parameters	One-step Quadratic		PD-IPM		Accelerated TVAL3 ($\beta = 32$)
1	$\lambda \equiv 1/\alpha$	1.26e-2		6.31e-4		1.13e-3
	RE	1.0022		1.0030		1.0012
	CPU Time	0.9681 Sec		1.7466 Sec		0.1423 Sec
	iterations	1		20		43
2	$\lambda \equiv 1/\alpha$	1e-2		5e-4		1e-3
	RE	1.0045		1.0052		1.0046
	CPU Time	1.0352 Sec		1.8261 Sec		0.1616 Sec
	iterations	1		20		48

Table 4. Evaluation of the optimal images of the golf balls.

Figs. 5(a), (b) and (c) show the optimal images of the first setup, and Figs. 5(d), (e) and (f) pertain to the second setup. Figs. 5(a) and (d) were calculated by the one-step quadric solver, Figs. 5(b) and (e) were reconstructed from the PD-IPM, and Figs. 5(c) and (f) correspond to the accelerated TVAL3. This figure indicates that the modified TVAL3 improved accuracy of images relative to the PD-IPM. In light of the color bars shown to the right of the images, TVAL3 provided sharper interfaces for both the setups. Furthermore, TVAL3 recovered shape of interfaces more accurately than the PD-IPM, especially in the second setup. However, it must be remembered that TV solvers are efficient in recovering large-scale inclusions, and the application of these solvers to recover small inclusions still remains a challenge in EIT.
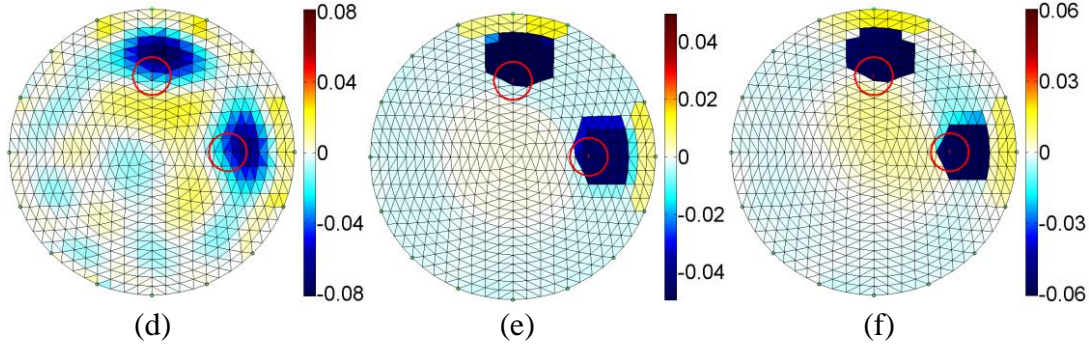

(a)   (b)   (c)
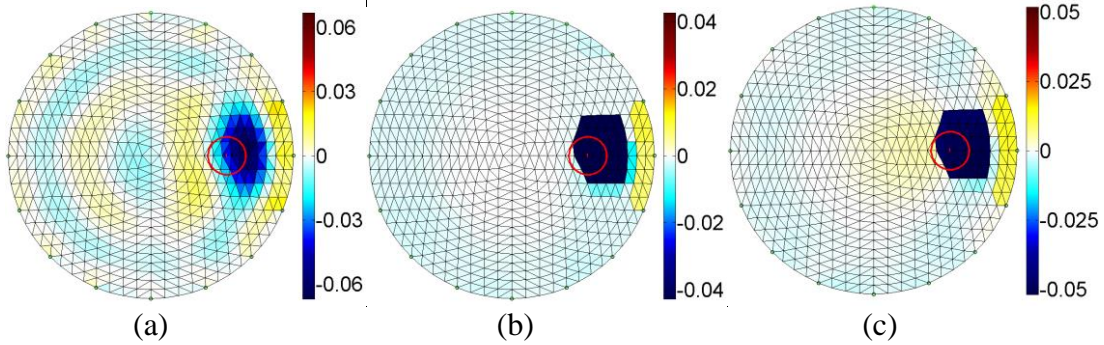
Fig. 5. The optimal images of the first setup computed by: (a) One-step Quadratic, (b) PD-IPM, (c) accelerated TVAL3, and the second setup computed by: (d) One-step Quadratic, (e) PD-IPM, (f) accelerated TVAL3.

4.2. Clinical in vivo imaging

The TV regularization, if it identifies inter-organ interfaces accurately, can play a significant role in clinical imaging. Such cases arise for example in detecting interface between the collapsed and ventilated volumes of an injured lung, the size of a tumor, etc. In what follows, the presented TV solvers are applied to two instances of clinical data that are available on the EIDORS website.

4.2.1. Lung (Human shallow breathing)

Sixteen ECG electrodes, which were connected to an EIT system, were equidistantly placed around the chest of an adult human, and data were measured according to the well-known adjacent strategy at 22 times. Here, we attempt to recover the difference between the first and 22nd frame of the lung data, as the 22nd frame is considered as the reference data on the EIDORS [40-c].

To cope with the measurement errors, the normalized difference scheme was applied to the solvers. The one-step quadratic algorithm was regularized by a smoothness penalty similarly to the previous subsection [40-c]. Since the true conductivity of the lungs was not available, the calculation of RE was impossible. The quadratic solver was applied by the regularization parameter used in the EIDORS for this data, i.e., $\lambda = 5e - 2$ [40-c]. Applying the TV solvers, the optimal regularization parameter was determined by applying a wide range of values and then characterizing the reconstructed images with respect to CNR, which does not depend on the true conductivity field. In light of the difference imaging, the CNR is calculated as

$$CNR = \frac{\left| \text{mean}_{IR} - \text{mean}_{BR} \right|}{\left(\dfrac{A_{IR}}{A_{Tot}} \text{var}_{IR} + \dfrac{A_{BR}}{A_{Tot}} \text{var}_{BR} \right)^{1/2}} . \tag{39}$$

Where, *IR* denotes the area encompassing the elements whose absolute conductivity exceeds one-fourth of the maximum absolute conductivity (inclusion), and *BR* denotes the remaining area. In addition, *A*, mean and var respectively, denote the area, the mean conductivity, and the variance of the conductivity over the defined regions [56]. The numerator of Eq. (39) determines the sharpness of the image, while the denominator measures how much the image deviates from being piecewise constant. In contrast with RE, CNR is a positive measure. This implies that the optimal image of the resulting curve is the point that yields the maximum CNR.

Table 5 in the top row first quantifies the one-step quadratic reconstruction, and then presents the optimal values resulting from the TV solvers, which are the maximal points of curves that plot the CNR against the applied regularization

parameters $\lambda \equiv 1/\alpha$. β was set to 16 in the TVAL3. The regularization parameters were chosen 21 values in the range $10^{-4} \le \lambda \equiv 1/\alpha \le 10^{-2}$. The results show that the accelerated TVAL3 was more tolerant than the PD-IPM in recovering images. This scheme was executed more rapidly than the PD-IPM as well; consider that the solvers were stopped by the same stopping criterion. Figs. 6(a), (b) and (c) respectively, show optimal images reconstructed by the quadratic, PD-IPM, and the accelerated TVAL3 solvers. The difference between Fig. 6(a) and the corresponding image in the EIDORS example is only due to the use of different color bars. A comparison between Figs. 6(b) and (c) demonstrates that the modified TVAL3 recovered lungs' boundaries with a lower distortion than the PD-IPM.
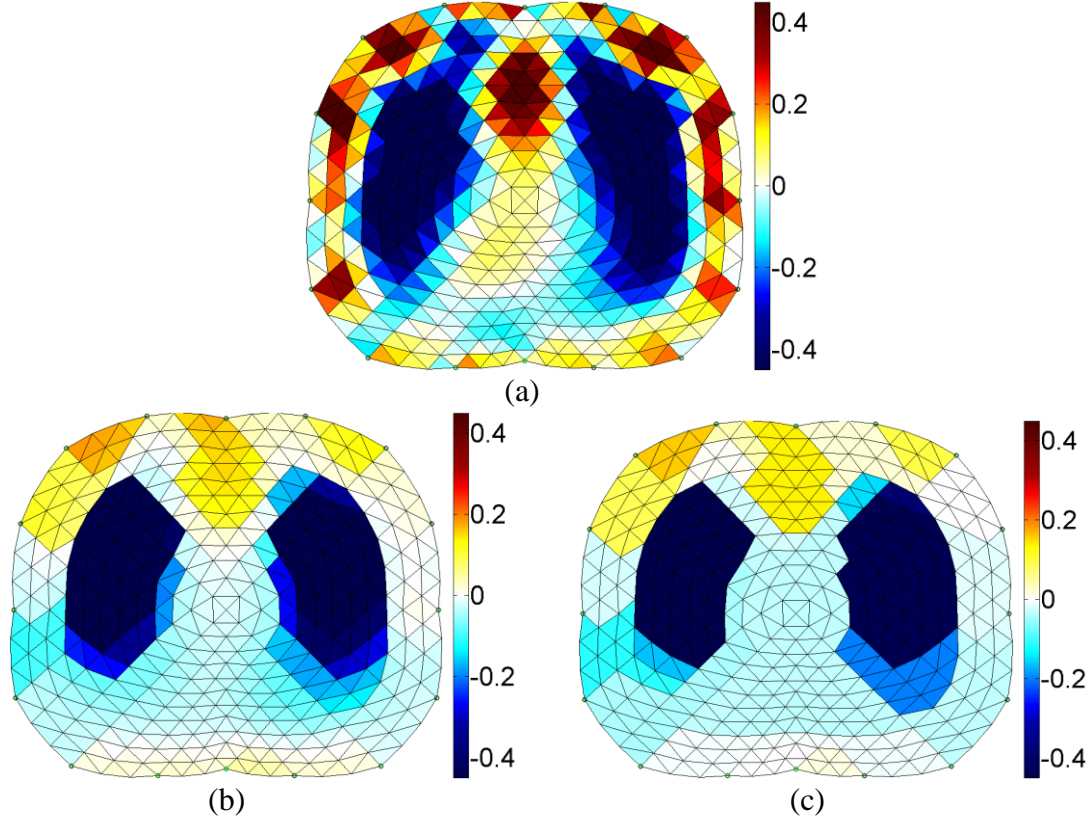

Fig. 6. The optimal images of human's lung reconstructed by: (a) one-step quadratic, (b) PD-IPM, and (c) accelerated TVAL3 solvers.

4.2.2. Gastric emptying

Sixteen electrodes were equidistantly installed around the abdomen of a human subject, and the reference data was measured from his empty stomach. 335 ml Coca-Cola was then fed to the subject. A set of data was measured after every five minutes. Here our aim is reconstruct the last frame of data, which was taken 60 minutes after drinking. The bottom row of Table 5 evaluates the optimal reconstructed images, which were calculated similarly to those of the lung data. This table confirms that the accelerated TVAL3 is faster and more accurate than the PD-IPM in reconstructing the optimal images. Figs. 7 (a), (b) and (c) respectively, exhibit the optimal images solved by the quadratic, PD-IPM, and the modified TVAL3 algorithms. Again the quadratic solver was applied similarly to the EIDORS example in [40-d]. Fig. 7 demonstrates that the accelerated TVAL3 solver produced a sharper optimal image than the PD-IPM with a smaller artifact.
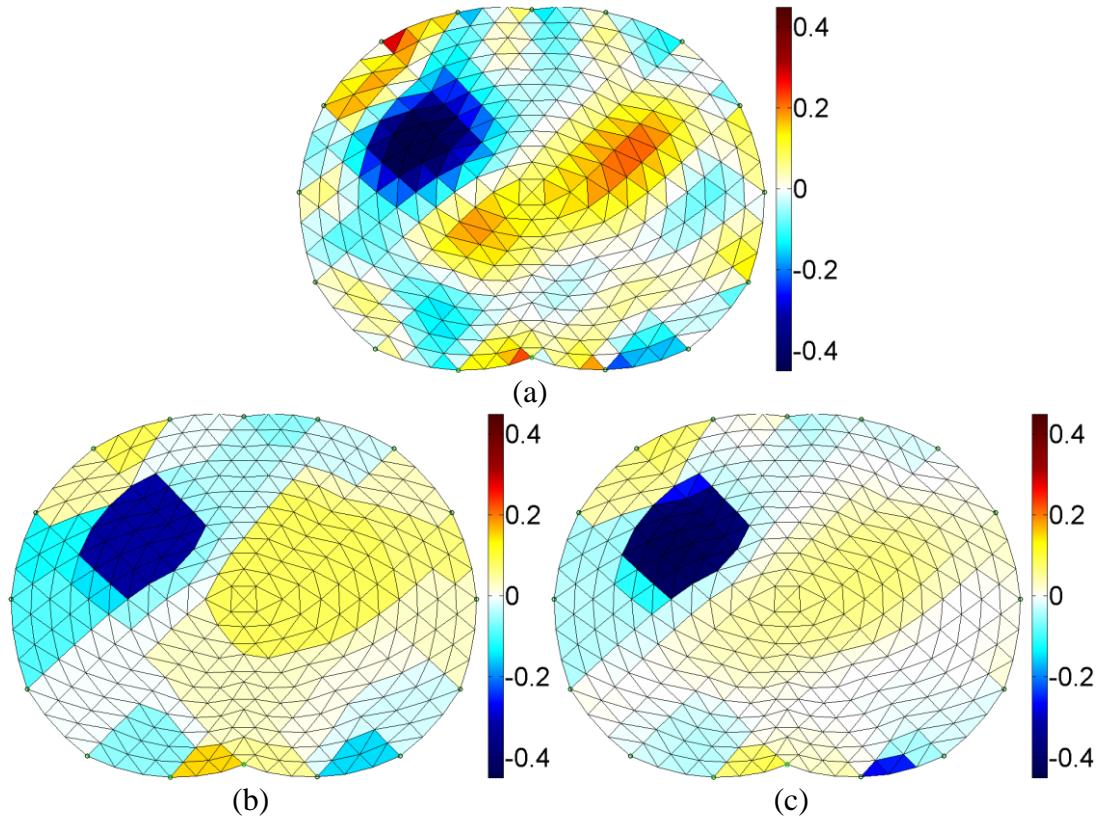
Fig. 7. The optimal images of the human's stomach, taken 60 minutes after drinking the Coca-Cola, reconstructed by: (a) one-step quadratic, (b) PD-IPM, and (c) modified TVAL3 solvers.

Setup	Parameters	One-step Quadratic	PD-IPM	Modified TVAL3 ($\beta=16$)
Lung (1st and 22nd frames)	$\lambda \equiv 1/\alpha$	5e-2	1e-3	5.01e-4
	CNR	3.2133	4.7873	5.1008
	CPU Time	0.7443 Sec	1.2383 Sec	0.1179 Sec
	iterations	1	14	39
Gastric (reference and 13th frame)	$\lambda \equiv 1/\alpha$	5e-2	1e-3	2.51e-4
	CNR	3.6228	3.6986	5.5432
	CPU Time	0.8142 Sec	1.3674 Sec	0.1252 Sec
	iterations	1	13	37

Table 5. Evaluation of the optimal images obtained from clinical data in EIDORS.

5. Discussion

The problem of reconstructing spatially varying conductivity distribution from a set of electrostatic measurements at the surface is severely ill-posed, even by reducing the size of the problem via transferring the conductivity field to a finite dimensional space [13]. Since there exist many conductivity fields which yield data that matches real data in the least square sense, the exact recovery of the conductivity field from a noisy data is not computationally tractable. Instead, the solution is restricted to *a*

priori assumption about the conductivity [12-14]. However, the measured data is typically insensitive to the high frequency contents of the conductivity profile. This permits different assumptions with various frequency features on the reconstructed image [23]. To regularize the problem, the deviation of the solution from the *a priori* assumption is penalized and augmented to the least square functional to be minimized. The smoothness penalties, which were employed since the inaugural studies in EIT, typically impose some unappealing blurriness on the reconstructed image [15]. Recently, the sparsity penalties have received much attention in EIT [18-21] thanks to their efficiency in recovering sparse conductivity fields, i.e., simple inclusions plus an unknown but uninteresting background [11]. Unfortunately, the sparse penalties cannot suitably deal with the sparsity of the gradient of the conductivity rather than the conductivity itself. So using the sparsity priors, the precise recovery of abrupt conductivity changes that provide sub-domain interfaces still remains a challenge.

In clinical EIT applications, a precise detection of sharp conductivity changes is essential in order to favorably describe organs' functions. The best approach to recover discontinuities over the domain is to regularize the inverse problem by the assumption that the conductivity field is piecewise constant. This assumption implies that the total variation of the conductivity distribution, the so-called TV functional, is minimal. The objective is thus to minimize the TV functional subject to the constraints imposed by the measured data [23]. As far as we know, the most commonly used TV solvers in EIT are the Lagged Diffusivity (LD) and the Primal-Dual Interior-Point-Method, which are available on the EIDORS website [40-a]. Borsic et al [39] showed that the PD-IPM outperforms LD in EIT. These solvers are based on second-order optimization, which significantly increases the execution time because of the need for computing and storing the Hessian. This precludes the application of these solvers to real-time monitoring of organs' functions. In addition, smoothing TV function to combat its non-differentiability at the origin imposes some numerical errors on the solution, and deleteriously affects the convergence of the algorithm [13-39].

In recent years, many modern TV algorithms were developed (cf. section 1). To address the errors arising from smoothing the TV function, a new class of TV solvers based on variable splitting technique has been proposed [50]. Applying a half-quadratic objective function, the solver requires the multipliers to extremely increase, which makes the problem very ill-posed [50-51]. To override this difficulty, an augmented Lagrangian function is proposed [51]. Accordingly, the problem is solved by alternative minimization of the objective function with respect to a slack variable and the gray-level image [51-52]. This algorithm is quite fast since it does not require the Hessian. It exhibits very good convergence rate as a result of penalizing the violation of the smoothing approximation on the TV function by means of the slack variable. The TVAL3 algorithm was proposed to attain these objectives, and has shown its great potential in high dimensional problems [51-52]. In this study, we first propose an accelerated version of TVAL3 based on the strategy proposed in [54], referred to as FISTA, and shows its great performance in TV minimization in EIT, compared to the existing TV solvers in EIT.

6. Conclusion

Although TV minimization plays an important role in preserving sharp transitions over the conductivity, the application of the state-of-the-art TV solvers to EIT remains

scarce. The existing TV solvers in EIT, e.g., PD-IPM or Lagged Diffusivity, are based on Newton's method, and are thus very time consuming. In addition, the numerical errors arising from smoothing the TV functional disallows a precise determination of interfaces from noisy data. This study proposed an accelerated version of TVAL3 algorithm [51-52], and tailored it to finite element domain for application in EIT. The spatial gradient of conductivity was weighted locally by length of edges between finite elements. The PD-IPM was considered as the benchmark since it is known the most robust TV solver applied to EIT. The results show that the accelerated TVAL3 outperforms PD-IPM with regard to both accuracy and speed.

References

[1] D.S. Holder, Electrical Impedance Tomography: methods, history and applications, Institute of Physics Publishing, 2004, pp. 3-64.

[2] R.H. Bayford, Bioimpedance Tomography (Electrical Impedance Tomography). Annu. Rev. Biomed. Eng, 8 (2006) 63-91.

[3] D.C. Barber and B.H. Brown Errors in reconstruction of resistivity images using a linear reconstruction technique, Clin. Phys. Physiol. Meas. 9 (1988) 101–4.

[4] J.F.P.J. Abascal, S. R. Arridge, D. Atkinson, R. Horesh, L. Fabrizi, M.D. Lucia, L. Horesh , R.H. Bayford, D.S. Holder, Use of anisotropic modelling in electrical impedance tomography; Description of method and preliminary assessment of utility in imaging brain function in the adult human head, NeuroImage 43 (2008) 258–268.

[5] A. Adler, J.H. Arnold, R. Bayford, A. Borsic, B. Brown, P. Dixon, T.J.C. Faes, I. Frerichs, H. Gagnon, Y. Gaerber, B. Grychtol, G. Hahn, W.R.B. Lionheart, A. Malik, R.P. Patterson, J. Stocks, A. Tizzard, N. Weiler, G.K. Wolf, GREIT: a unified approach to 2D linear EIT reconstruction of lung images Physiol. Meas. 30(2009) 35–55.

[6] M. Balleza, N. Calaf, T. Feixas, M. Gonzalez, D. Anton, P.J. Riu, P. Casan, Measuring breathing pattern in patients with chronic obstructive pulmonary disease by electrical impedance tomography, Arch Bronconeumol. 45(2009) 320-24.

[7] A. Javaherian, M. Soleimani, Compressed sampling for boundary measurements in three-dimensional electrical impedance tomography. Physiol. Meas. 34 (2013)1133–1150.

[8] M.C. Kim, S. Kim, K.Y. Kim and Y.J. Lee, Regularization methods in electrical impedance tomography technique for the two-phase flow visualization, Int. Comm. Heat Mass Transfer, 28 (2001), 773-782.

[9] O.P. Tossavainen, M. Vauhkonen, V. Kolehmainen, K.Y. Kim, Tracking of moving interfaces in sedimentation processes using electrical impedance tomography, Chemical Engineering Science 61 (2006) 7717 – 7729.

[10] U.Z. Ijaz, J.H. Kim, A.K. Khambampati, M.C. Kim, S. Kim, K.Y. Kim, Concentration distribution estimation of fluid through electrical impedance tomography based on interacting multiple model scheme, Flow Measurement and Instrumentation 18 (2007) 47–56.

[11] B. Jin, P. Maass. An analysis of electrical impedance tomography with applications to Tikhonov regularization, ESAIM: COCV. 18(4) 2012 1027-48.

[12] A. Adler and R. Guardo, Electrical impedance tomography: Regularized imaging and contrast detection, IEEE Trans. Biomed. Eng. 15(1996) 170-9.

[13] A. Borsic, Regularisation Methods for Imaging from Electrical Measurements, Phd thesis, Oxford Brooks university 2002.

[14] W.R.B. Lionheart, EIT reconstruction algorithms: pitfalls, challenges and recent developments Physiol. Meas. 25 (2004)125–42.

[15] A. Javaherian, A. Movafeghi, R. Faghihi, Reducing negative effects of quadratic norm regularization on image reconstruction in electrical impedance tomography, Appl. Math. Model. 37(8) (2013) 5637-5652.

[16] F. Santosa and W.W. Symes, Linear inversion of band-limited reflection seismograms, SIAM J. Sci. Statist. Comput., 7(4) (1986) 1307–1330.

[17] D.L. Donoho, Compressed sensing. IEEE Trans. Inf. Theor. 52 (2006) 1289–1306.

[18] B. Jin, Y. Zhao and P. Maass, A reconstruction algorithm for electrical impedance tomography based on sparsity regularization. Internat. J. Numer. Methods Engrg. (2011), DOI: 10.2002/nme.3247.

[19] B. Jin, T. Khan, P. Maass. A reconstruction algorithm for electrical impedance tomography based on sparsity regularization. International Journal for Numerical Methods in Engineering 89(3) (2012) 337-353.

[20] A. Javaherian, M. Soleimani, K. Moeller, A fast time‑difference inverse solver for 3D EIT with application to lung imaging, Med. Biol. Eng. Comput. 2016, in press.

[21] A. Javaherian, M. Soleimani, K. Moeller, Sampling of finite elements for sparse recovery in large scale 3D electrical impedance tomography, Physiol. Meas. 36(1) (2015) 43-66.

[22] E. Cand`es, J. Romberg, T. Tao, Robust uncertainty principles: Exact signal reconstruction from highly incomplete frequency information, IEEE Trans. Inform. Theory, 52(2) (2006) 489–509.

[23] D.C. Dobson and F. Santosa, An image enhancement technique for electrical impedance tomography, Inv. Probl., 10 (1994) 317–334.

[24] K. Van den Doel, U.M. Ascher, Dynamic level set regularization for large distributed parameter estimation problems, University of British Columbia, Vancouver, 2007.

[25] K. Van den Doel, U.M. Ascher, A. Leitao, Multiple level sets for piecewise constant surface reconstruction in highly ill-posed problems, University of British Columbia, Vancouver, 2009.

[26] E.T. Chung., T.F. Chan, X.C. Tai, Electrical impedance tomography using level set representation and total variational regularization, J. Comput. Phys. 205 (2005) 357–372.

[27] M. Soleimani, W.R.B. Lionheart, O. Dorn, Level set reconstruction of conductivity and permittivity from boundary electrical measurements using experimental data, Inverse Problems Sci. Eng. 14 (2006) 193-210.

[28] P. Rahmati, M. Soleimani, S. Pulletz, I. Frerichs, A. Adler, Level-set-based reconstruction algorithm for EIT lung images: first clinical results, Physiol. Meas. 33 (2012) 739-750.

[29] L. Rudin, S. Osher, and E. Fatemi, Nonlinear total variation based noise removal algorithms, Physica D, 60 (1992) 259–268.

[30] R. Acar, C.R. Vogel, Analysis of bounded variation penalty methods for ill-posed problems, Inv. Probl., 10 (1994), 1217–1229.

[31] T.F. Chan, G. Golub, P. Mulet, A nonlinear primal dual method for TV-based image restoration, UCLA CAM Tech. Rep. 95-43, 1995.

[32] T.F. Chan, H.M. Zhou, and R.H. Chan, A continuation method for total variation denoising problems, UCLA CAM Tech. Rep. 95-18, 1995.

[33] C.R. Vogel, M.E. Oman, Iterative methods for total variation denoising, SIAM J. Sci. Comput., 17 (1996), 227–238.

[34] T.F. Chan and P. Mulet, Iterative methods for total variation restoration, UCLA CAM Tech. Rep., 1996, 96-38.

[35] D.C. Dobson, C.R. Vogel, Convergence of an iterative method for total variation denoising, SIAM J. Numer. Anal., 43 (1997) 1779–1791.

[36] V. Kolehmainen, Novel Approaches to Image Reconstruction in Diffusion Tomography, Ph.D. dissertation, Dept. Appl. Phys., Kuopio Univ., Kuopio, Finland, 2001.

[37] L. Rondi, F. Santosa, Enhanced electrical impedance tomography via the Mumford-Shah functional. ESAIM: COCV, 6 (2001) 517-538.

[38] C.R. Vogel, Nonsmooth regularization, in Inverse Problems in Geophysical Applications, H.W. Engl, A.K. Louis, and W. Rundell, Eds. Philadelphia, PA: SIAM, 1995.

[39] A. Borsic, B.M. Graham, A. Adler, W.R.B. Lionheart, In vivo impedance imaging with total variation regularization, IEEE Trans. on Med. Imag., 29(1) (2010) 44-54.

[40] EIDORS 3.5, Electrical Impedance Tomography and Diffuse Optical Tomography Reconstruction Software, 2016
http://eidors3d.sourceforge.net/tutorial/adv_image_reconst/total_variation.shtml (a)
http://eidors3d.sourceforge.net/data_contrib/cg_deforming_tank_phantom/cg_deforming_tank_phantom_02.shtml (b)
http://eidors3d.sourceforge.net/tutorial/lung_EIT/tutorial310-lung-images.shtml (c)
http://eidors3d.sourceforge.net/tutorial/lung_EIT/tutorial410-stomach-images.shtml (d)

[41] D. Goldfarb, W. Yin, Second-order cone programming methods for total variation based image restoration, SIAM Journal on Scientific Computing, vol. 27(2) (2005) 622–645.

[42] E. Cand`es, T. Tao, Decoding by linear programming, IEEE Trans. Inform. Theory, 51(12) (2005) 4203–4215.

[43] E. Cand`es, T. Tao, Near optimal signal recovery from random projections: Universal encoding strategies, IEEE Trans. on Inform. Theory, 52 (12) (2006) 5406–5425.

[44] E. Cand`es, J. Romberg, T. Tao, Robust uncertainty principles: Exact signal reconstruction from highly incomplete frequency information, IEEE Trans. Inform. Theory, 52(2) (2006) 489–509.

[45] J. Bioucas-Dias, M. Figueiredo, A new TwIST: Two-step iterative thresholding algorithm for image restoration, IEEE Trans. Imag. Process., 16 (12) (2007) 2992–3004.

[46] J. Bioucas-Dias, M. Figueiredo, Two-step algorithms for linear inverse problems with non-quadratic regularization, IEEE International Conference on Image Processing–ICIP2007, San Antonio, TX, USA, September 2007.

[47] A. Chambolle, An algorithm for total variation minimization and applications, J. Math. Imaging. Vis, 20 (2004), 89–97.

[48] S. Becker, J. Bobin, E. Cand`es, NESTA: A fast and accurate first-order method for sparse recovery, Technical Report, California Institute of Technology, 2009.

[49] Yu. Nesterov, Smooth minimization of non-smooth functions, Math. Program., Ser. A 103 (2005) 127–152.

[50] Y. Wang, J. Yang, W. Yin, Y. Zhang, A new alternating minimization algorithm for total variation image reconstruction, SIAM J. Imag. Sci. 1(4) (2008) 248–272.

[51] C. Li. An efficient algorithm for total variation regularization with applications to the single pixel camera and compressive sensing, Master thesis, Rice University, Houston, Texas, 2009.

[52] http://www.caam.rice.edu/~optimization/L1/TVAL3/

[53] J. Barzilai, J.M. Borwein, Two-point step size gradient methods, IMA J. Numer. Anal., 8 (1988) 141–148.

[54] A. Beck, M. Teboulle, A Fast Iterative Shrinkage-Thresholding Algorithm for Linear Inverse Problems, SIAM J. Imaging Sciences 2 (2009) 183-202.

[55] B. Graham, A. Adler, Electrode placement configuration for 3D EIT Physiol. Meas. 28 (2007) 29-44.

[56] T.K. Bera, S.K. Biswas, K. Rajan, J. Nagaraju, Improving image quality in electrical impedance tomography (EIT) using projection error propagation-based regularization (PEPR) technique: A simulation Study, j. Electr. Bioimp., 2 (2011) 2–12.